Direct Antenna Modulation for High-Order Phase Shift Keying

Stephen Henthorn, Kenneth Lee Ford, *Senior Member, IEEE*, and Timothy O'Farrell, *Senior Member, IEEE*

***Abstract*— An antenna capable of directly phase modulating a radio frequency (RF) carrier is discussed, designed, and measured as both an antenna and a modulator. Access point densification for the Internet of Things will be expensive in part due to the cost and inefficiency of amplifying waveforms with large peak-to-average power ratios for downlink transmission. Directly modulating at the antenna means only a carrier wave has to be amplified, reducing the cost of densification. Here, reconfigurable frequency selective surfaces are suggested as phase modulators. The design process for producing a phase modulating antenna is detailed, and a prototype is fabricated that is capable of up to 8-PSK modulation with 5.3 dB variation in constellation points and a peak gain of 2.3 dB. When implemented in an end-to-end communications system, the antenna exhibits only 1.5 dB drop in performance compared with instrument grade modulation in an additive white Gaussian noise (AWGN) channel.**

***Index Terms*— Cellular radio, continuous phase modulation, frequency selective surfaces (FSSs), phase shift keying(PSK), reconfigurable antennas.**

I. Introduction

CONNECTING millions of devices in smart, reconfigurable networks has the possibility to change the way public service delivery, civic infrastructure and industry operate. Developing the technology and communications infrastructure for this Internet of Things (IoT) is a major challenge [1]. The main approaches to support so many devices have been either narrowband (NB), such as NB-IoT and Weightless [2], [3], or wideband, such as Ingenu and long range wireless access network (LoRaWAN) [4], [5]. Wideband technologies have the advantage of being interference-resilient, allowing operation in licensed or unlicensed bands, and are flexible in terms of the number of devices and data rates they can support [6]. This is particularly of interest on the IoT downlink, where many devices must have a near-constant link to enable smart network reconfiguration and resource allocation [7].

However, the wideband downlink approach would require an expansion of network infrastructure, increasing the number of base stations to support the millions of new connected devices. This increases the installation and running costs of the network. A large proportion of this cost is the downlink transmitter, and in particular the power amplifier (PA) [8], [9]. This is because, in traditional radio transmitter architectures, modulation occurs at low power, and the whole signal is amplified to a relatively high power [Fig. 1(a)] [10]. The wideband IoT downlink signal would have a significant peak-to-average power ratio, which the PA must amplify without distortion. In order to do this, expensive linear PAs are operated at back-off, resulting in a drop in efficiency and increasing operating costs [11].

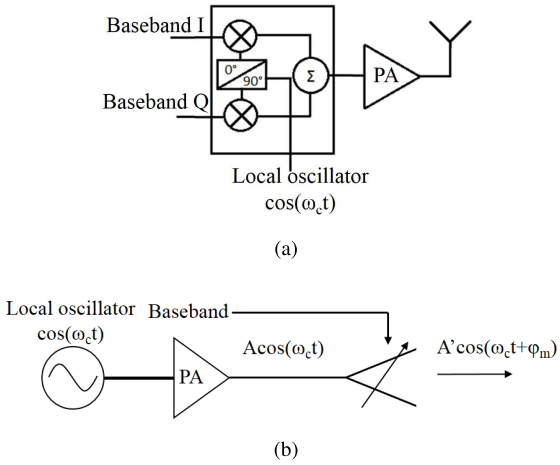

Fig. 1. (a) Block diagram of a conventional homodyne quadrature transmitter. (b) Concept diagram of a DAM transmitter using a reconfigurable antenna.

Several different approaches have been taken to overcome these issues. Constant envelope modulation techniques have been utilized in order to avoid distortion even when using nonlinear PAs, for example, Gaussian minimum shift keying (GMSK) which was used in the global system of mobile communications (GSM)/enhanced data for GSM evolution (EDGE) cellular standards [12], [13]. Another research topic is the PA design, in particular work on Doherty amplifiers [14]. At least two amplifiers are biased independently to amplify the lower voltages and peaks of the input signal separately, allowing efficiency to be maintained in back-off. Other developments in PA design for communications include the Chireix amplifier, which separates the input signal into distinct constant envelope signals, amplifies them separately, then combines them [15]. Efficiency is improved particularly at lower input amplitudes, though this is again at the cost of greater complexity. Combinations of these approaches have also been explored [16].

Recently, ways of avoiding these problems by changing the fundamental transmitter architecture have been explored. In these studies, only the carrier wave is amplified by the

Manuscript received December 7, 2018; revised July 22, 2019; accepted August 5, 2019. Date of publication August 23, 2019; date of current version January 3, 2020. This work was supported in part by Industrial Sponsors NEC Telecom Modus and BT Research through the EPSRC iCASE Award and in part by EPSRC under Grant EP/M013723/1 [Frequency Agile Radio (FARAD)]. *(Corresponding author: Stephen Henthorn.)*

The authors are with the Department of Electronic and Electrical Engineering, The University of Sheffield, Sheffield S10 2TN, U.K. (e-mail: sdhenthorn1@sheffield.ac.uk; l.ford@sheffield.ac.uk; t.ofarrell@sheffield.ac.uk).

Color versions of one or more of the figures in this article are available online at http://ieeexplore.ieee.org.

Digital Object Identifier 10.1109/TAP.2019.2935136

PA, and the data signal is modulated directly on to the radio frequency (RF) wave using electromagnetic techniques at the antenna [Fig. 1(b)]. This is known as direct antenna modulation (DAM). The first instance of this was integrating a Schottky diode between the radiating element and the ground plane of a patch antenna, allowing time domain modulation [17]. This concept was further developed by using p-i-n diodes, and showing how these could be used to allow a patch antenna to transmit signals more broadband than its own bandwidth [18], [19]. A similar approach for ultrawideband on–off keying (OOK) with a patch antenna is described in [20].

DAM techniques have also been developed to produce directional modulation. In [21], a single element driven by a RF carrier wave is surrounded by passive reflectors with integrated p-i-n diodes. Switching these diodes allows for production of arbitrary constellations in a given transmit direction, with receivers at other locations seeing a significantly distorted constellation. This work is further developed in [22], while further work using arrays of elements driven by one source but using phase shifters to produce constellations has also been explored [23], [24].

Metamaterials have also been suggested as possible modulators in a DAM transmitter. Kiani *et al.* [25] suggest integrating a bandpass reconfigurable frequency selective surface (FSS) with p-i-n diodes, as in [26], to switch the FSS between transmission and reflection in order to produce amplitude shift keying (ASK) modulation. There is a suggestion that this could allow high rate modulation at millimeter wave and terahertz transmit frequencies. More recently, an electrically large reflective metasurface loaded with varactor diodes has been shown to produce order eight phase shift keying (PSK) modulation when illuminated by a plane wave [27].

The authors have previously proposed using transmissive FSS with integrated varactor diodes allowing control of the transmitted phase [28]. A proof-of-concept prototype capable of producing quadrature phase shift keying (QPSK) modulation is shown in [29], which shows modulation using this prototype can achieve a drop of only 4 dB in SNR performance when using spread spectrum techniques. However, it is only capable of low order modulation and has low gain.

Similar work using FSS to vary transmitted phase has also been explored to produce beamsteering antennas. Using bandpass FSS which change the transmitted phase in order to beamform have been explored, creating a planar lens either in front of an antenna, as in [30], or incorporated in a resonant cavity, as in [31]. Again, there are proposals to make these reconfigurable by varying capacitance [32], [33] or by switching p-i-n diodes [34], [35]. Each of these techniques requires individual control of each unit cell.

This article presents a full characterization and system implementation of an antenna capable of phase DAM. By increasing the number of FSS layers, improvement over previous proof-of-concept demonstrations of FSS DAM has been achieved with up to at least 8-PSK modulation. The effects of different contributions of loss are examined, as are the effects of varying key design parameters. The DAM communications system in this article is also improved, using a balancing code rather than direct sequence spread spectrum (DSSS) for amelioration of systematic distortions. This, along with the FSS design developments described above, produces a large improvement in the data rate, efficiency and bit error rate (BER) over previous work. In Section II, the concept and some challenges of using FSS for PSK DAM is described in Section II. In Section III, the modulating antenna is designed and simulated in CST Microwave Studio, from unit cell to a FSS integrated antenna. The fabrication process and antenna measurements are described in Section IV. Finally, in Section V the modulating antenna is incorporated into an end-to-end communications system, with BER measurements shown for binary phase shift keying (BPSK), QPSK and 8-PSK modulation in additive white Gaussian noise (AWGN).

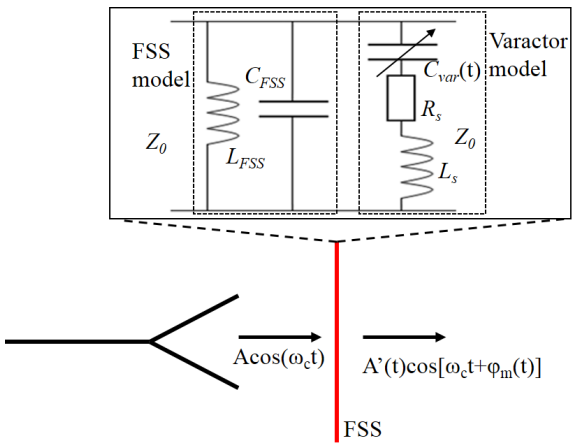

Fig. 2. Concept of DAM using a reconfigurable bandpass FSS.

II. Direct Antenna Modulation Using Frequency Selective Surfaces

The concept of using FSS for directly modulating at the antenna is shown in Fig. 2. An FSS is placed in front of a passive antenna, transmitting a carrier wave at frequency ω_c with amplitude A. The FSS acts a bandpass filter, as shown by the equivalent circuit described in [36], with some inductance L_{FSS} and capacitance C_{FSS} defining its resonant frequency. Variable capacitors are integrated with the FSS, adding in parallel a reconfigurable capacitance, C_{var}, in series with some parasitic resistance R_s and inductance L_s. This reconfigurable capacitance allows tuning of the FSS center frequency.

When the carrier wave is incident on the FSS and ω_c is within the FSS passband, a phase change ϕ_m is produced, with some reduction in magnitude to A'. Changing the center frequency of the FSS allows control of ϕ_m with only small changes in A'. This forms the basis of a phase modulator operating at the antenna.

III. Design of a Phase Modulating Antenna

In this section, the design process of a FSS-based modulating antenna is discussed. For demonstration, the antenna will be capable of a single linear polarization and operate at 1.8 GHz.

A. Frequency Selective Surface Design for DAM

In order to produce arbitrary PSK modulation, the FSS must be able to produce 360° phase change with a minimum of

variation in magnitude. Also, in real-world implementation, the FSS may have to modulate signals with an oblique angle of incidence and operate effectively in a limited space. As such, a broadband reconfigurable bandpass FSS design with stability over a reasonable range of angles of incidence should be chosen. A square loop slot design was chosen for these reasons, as well as its relatively small cell size for a given resonant frequency [36].

To achieve the arbitrary phase change required for PSK modulation, the devices reconfiguring the FSS should allow fine control of the resonant frequency. They should also have minimal loss, acceptable linearity and, for wideband modulation, be capable of switching rates in the MHz. Variable capacitors allow continuous or near-continuous reconfigurability over a certain range, and types such as microelectromechanical systems (MEMS), barium strontium titanate (BST) tunable capacitors and liquid crystal capacitors have been demonstrated for use on FSS [37]–[39]. While MEMS and other digital capacitors have high linearity and low equivalent series resistances (ESRs), they have slow switching speeds and require complicated bias networks. BST capacitors are low loss, but due to their tuning mechanism the maximum switching rates with current commercial devices is in the kHz, while liquid crystal capacitors are in infancy. As such, due to their fast switching speeds, varactor diodes were chosen. In particular, the 1SV280 diode was chosen, due to its low ESR of 0.44 Ω and low capacitances. The model of the varactor used is shown in Fig. 2, with $R_s = 0.44\ \Omega$, $L_s = 0.6$ nH, and $C_{var} = 1$–4 pF. For a single linear polarization, diodes need only be integrated in line with the E-field of the incident wave, as shown in the final design of the unit cell [Fig. 3(a)].

Square-loop unit cells can be designed for a certain resonance using the equivalent circuit technique described in [36]. This describes the resonance of an FSS as some inductance L_{FSS} and some capacitance C_{FSS} in terms of the unit cell dimensions. Assuming a wave of normal incidence, the inductive impedance X_L and capacitive susceptance B_C can be calculated as follows:

$$\frac{X_L}{Z_0} = \frac{(s+2g)}{p} F(p, 2g, \lambda) \tag{1}$$

$$\frac{B_C}{Z_0} = \frac{(4s+8g)}{p} F(p, p-s-2g, \lambda) \tag{2}$$

where p, s, and g are the period, inner patch size, and loop thickness, respectively [Fig. 3(a)]. Function F is defined as

$$F(p, w, \lambda) = \frac{p}{\lambda}\left[ln\left(cosec\left(\frac{w\pi}{2p}\right)\right) + G(p, w, \lambda)\right] \tag{3}$$

where

$$G(p, w, \lambda) = \frac{1}{2}\frac{(1-\beta^2)^2\left[\left(1-\frac{\beta^2}{4}\right)(A_+ + A_-) + 4\beta^2 A_+ A_-\right]}{\left(1-\frac{\beta^2}{4}\right)+\beta^2\left(1+\frac{\beta^2}{2}-\frac{\beta^2}{8}\right)(A_+ + A_-)+2\beta^6 A_+ A_-} \tag{4}$$

$$A_\pm = \frac{1}{\sqrt{1 \pm \frac{p^2}{\lambda^2}}} - 1 \tag{5}$$

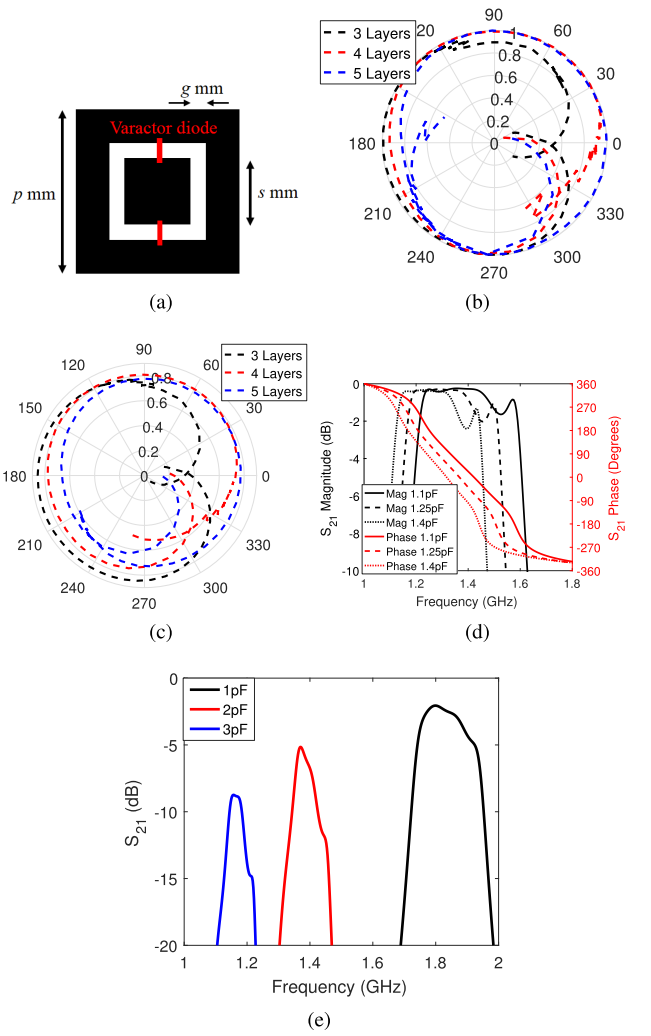

Fig. 3. (a) Schematic of reconfigurable FSS unit cell. (b) Free-space simulation of lossless FSS S_{21} with changing capacitance. (c) Free-space simulation of lossy FSS S_{21} with changing capacitance. (d) Free-space simulation of four-layer lossy FSS S_{21} with values $p = 14$ mm, $s = 12$ mm, $g = 0.6$ mm. (e) Free-space simulation of same FSS S_{21} over broad tuning range.

and

$$\beta = \frac{sin(\pi w)}{2p}. \tag{6}$$

The calculated X_L and B_C can then be used to find the resonant frequency of the FSS for a given geometry. When varactor diodes are integrated onto the FSS, the equivalent circuit becomes as shown in the detail of Fig. 2.

In order to achieve 360° of phase change, a multi-layer FSS is required. To find the appropriate number of layers, the square loop design in Fig. 3(a) was simulated in CST with Floquet boundaries in free space while varying the diode capacitance, with the S_{21} at 1.8 GHz recorded. The simulation used values $p = 15$ mm, $s = 12$ mm and $g = 0.6$ mm, and included a 1.6 mm thick substrate of FR4, with relative permittivity of $\epsilon_r = 4.4$ on each layer, and with spacings between the layers of $\lambda_0/4 = 41.7$ mm. The diodes were modeled as lumped elements with series inductance of $L_s = 0.6$ nH, series resistance $R_s = 0.44\ \Omega$ and a potential capacitance range

of $C_{var} = 1$–4 pF (Fig. 2). When a lossless substrate and lossless diodes were used, Fig. 3(b) is produced, showing that three layers has 5.3 dB variation in transmitted magnitude over 360° phase change, four layers has 2.9 dB variation, and five layers has 1.7 dB variation. These values are larger than the theoretical limit discussed in [40], which gives 1 dB variation for a four layer FSS. The discrepancy is due to the assumption for analysis in [40] that a single substrate material of $\epsilon_r = 1$ fills all the space between FSS layers, which does not hold when using any practical substrate with air gaps between layers. Furthermore, any losses due to tuning are not considered in [40]. Despite this, the simulations performed suggest that that more layers provide better modulation performance.

However, adding a substrate loss tangent of $\tan\delta = 0.025$ and diode ESR of 0.44 Ω to the model produces Fig. 3(c). This shows that the magnitude variation with phase and the total loss through the FSS are affected by the increase in loss. For four layers, the variation is 3.1 dB with a minimum loss of 1.8 dB, while for five layers the variation is 1.7 dB and the minimum loss is 2.3 dB. As such, while increasing the number of layers reduces the amount of magnitude variation with phase change, it also increases the total loss through the FSS. This tradeoff must be considered in the antenna design process. In this case, over the 315° required for an 8-PSK constellation, both five and four layer simulations show 1.4 dB variation. As such, a four layer design was chosen, and the simulated S_{21} of this design in free space is shown against frequency in Fig. 3(d). It should be noted that increasing the diode capacitance decreases the maximum S_{21} of the FSS [Fig. 3(e)]. This is because, at higher capacitances, the impedance of the diodes reduces at a given frequency, allowing more current to pass through. This then increases the I^2R losses in the diode resistance R_s. Furthermore, R_s in varactor diodes is smaller at lower capacitances [41], though this has not been included in the simulation model here. As such, to minimize transmission loss, the FSS should be designed to operate at low capacitances.

B. Antenna Design

In order to operate in a practical transmitter, the modulating FSS must be combined with an antenna. A free-space solution, with an element placed behind the multi-layered FSS, was found to be impractical due to the large physical size of FSS required to prevent the carrier diffracting around the FSS. As such, the FSS was integrated into a rectangular waveguide structure, ensuring all signals pass through all layers of the FSS. To inject RF into the waveguide, a monopole feed of length l is extended from an SMA connector and placed some distance from the FSS, here 57 mm [Fig. 4(a)]. A cavity backing is added $\lambda/4$ away from the monopole to ensure all the energy goes through the FSS, creating the final antenna design shown in Fig. 4.

However, in a waveguide solution the FSS behaves differently from the free space case, due to the change in wave impedance and the longer wavelength at 1.8 GHz inside the waveguide. The FSS must be finite-sized, with the strongest E-field at the center of the x-plane [42]. Fig. 5(a) shows the normalized polar signal transmitted by antennas with

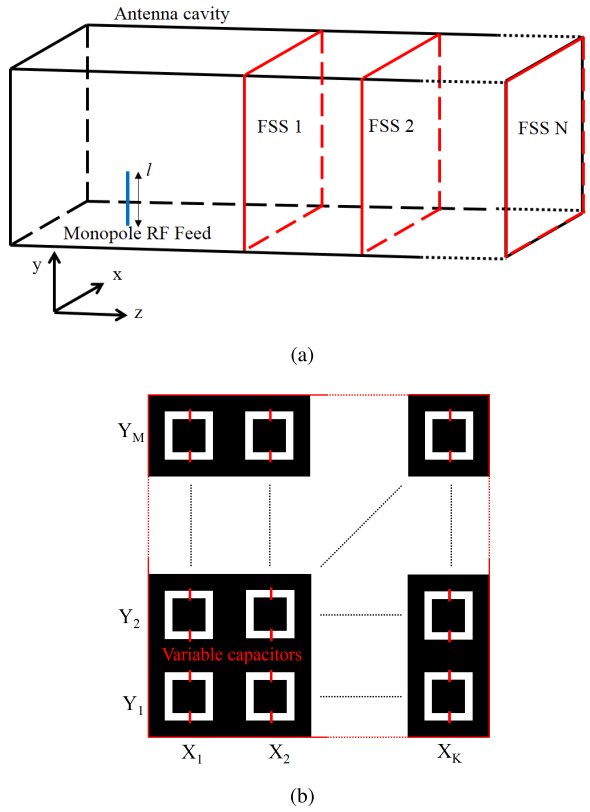

Fig. 4. Diagrams of modulating antenna concept. (a) 3-D antenna structure. (b) FSS structure in antenna.

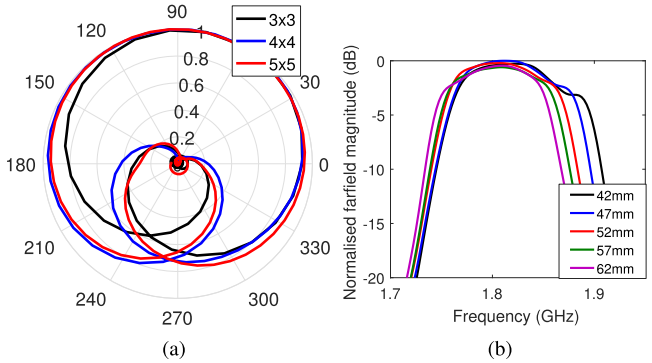

Fig. 5. Simulated antenna against frequency for $W = 112.5$ mm. (a) Polar far-field magnitude for different $M \times K$ numbers of unit cells at 1.5 pF. (b) Far-field magnitude with different spacings between FSS layers $d = 35$ mm.

differently sized FSSs, with the unit cell size held constant. A square configuration, with $M = K$, was chosen for symmetry. A 3×3 FSS has potential variation of 4.8 dB across 360°, which is larger than expected due to the FSS being spatially undersampled. However, for 4×4 and 5×5 configurations, the performance is consistent, with 2.9 dB variation. Using smaller numbers of unit cells reduces the number of diodes required for operation. However, it was found that for operation at 1.8 GHz while maintaining an acceptable antenna width of approximately 0.6λ, a 5×5 arrangement was required to have tuning capacitances in the low loss, low capacitance end of the chosen 1SV280 diode's tuning range.

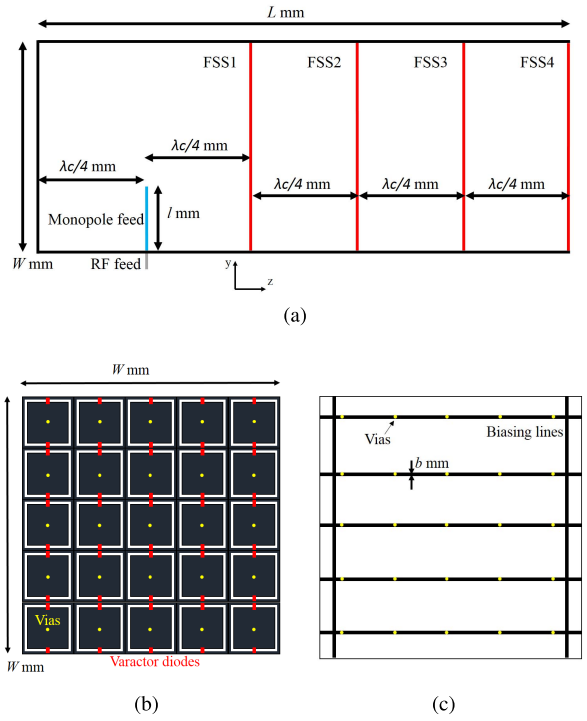

Fig. 6. Diagrams of antenna design. (a) Side view. (b) Front view. (c) Bias lines on reverse of FSS.

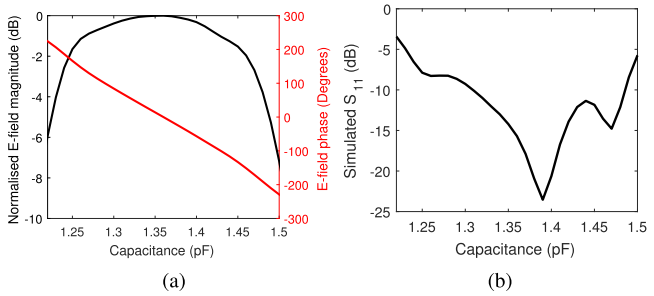

Fig. 7. Simulated antenna with varying capacitance. (a) Far-field magnitude and phase. (b) S_{11}.

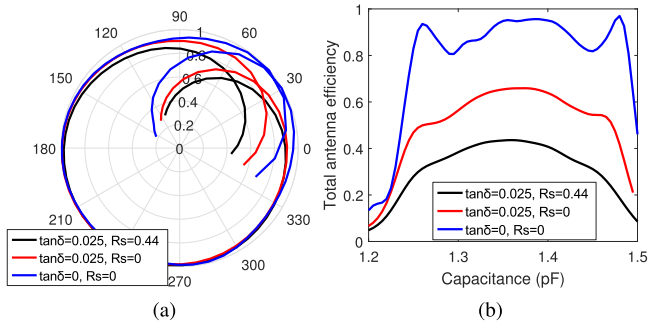

Fig. 8. Simulated antenna with varying capacitance for various loss configurations. (a) Polar plot of antenna far-field. (b) Total efficiency.

The optimal spacing between layers of the FSS was also explored. Using the equivalent circuit analogy, to provide the flattest filter response a transmission line of a quarter of a wavelength is required between each LC combination. However, within the cavity a quarter of a wavelength at transmit frequency is neither what it would be in free space, $\lambda_0/4$, nor the theoretical wavelength in an infinitely long square waveguide of size W, $\lambda_g = \lambda_0/\sqrt{1-(\lambda_0/2W)^2}$. Instead, it will be somewhere in between. In order to find this cavity wavelength λ_c, the full antenna structure was simulated with varying spacings at a fixed capacitance. Results for a waveguide of $W = 112.5$ mm and length $L = (5/4)\lambda_c$ is shown in Fig. 5(b), with the flattest response being the optimum, here $\lambda_c/4 = 57$ mm. Combinations of different spacings between FSS layers were also explored, but did not show any improvement in passband flatness.

The antenna also requires a biasing network to ensure all diodes are biased at the same time by the same voltage. However, this network should be designed to minimize the impact on the transmitted wave. As such, the design shown in Fig. 6(c) is used, with most of the bias lines with width $b = 1$ mm running horizontally, orthogonal to the incident E-field. The vertical lines are placed only 5.5 mm from the edge of the FSS, so that they are in a region where the E-field is relatively weak. Vias are used to connect the central patches of the FSS unit cells to the bias network. The bias lines add an upward shift of approximately 15 MHz to the center frequency of the FSS due to the added inductance, as well as an additional loss of 0.12 dB.

The final antenna design is shown in Fig. 6. The antenna is designed to operate in the licensed mobile band at 1.8 GHz, in line with expectations of using licensed mobile bands for IoT applications [43]. A 5×5 FSS was chosen with $p = 22.5$ mm, $s = 15$ mm, and $g = 1$ mm, with the latter chosen to fit the diode footprint [Fig. 6(b)]. This gives a cavity size $W = 0.675\lambda = 112.5$ mm and so optimum spacing $\lambda_c/4 = 57$ mm and probe length $l = 35$ mm. This is then simulated in CST with varying capacitance, with the diode assumptions given in Section III-B [Fig. 7(a)]. The capacitance range of the passband is between 1.2 and 1.5 pF at the low tuning end of the 1SV280, minimizing loss in the varactor diodes. The phase change in the passband is greater than 360°, and the expected magnitude variation across this is 2.7 dB. 1.3 dB of the variation can be attributed to the diodes' ESR, while 0.3 dB is due to losses in the FSS substrate [see Fig. 8(a)].

The simulated S_{11} is shown in Fig. 7(b), showing less than -10 dB match the majority of the passband, and -6 dB match for the whole of it, from 1.23 to 1.49 pF. This variation occurs due to the changing filter response of the FSS inside the antenna as the capacitance changes. The variation could be reduced by using a matching network, but for demonstration purposes the performance was deemed acceptable. The effects of varying the length l of the monopole feed while capacitance is held at 1.35 pF is shown in Fig. 9(a). This shows that a monopole feed length of $l = 35$ mm performs best at the center of the filter response. The simulated total efficiency is shown in Fig. 8(b), showing a maximum 46% efficiency. Simulation also shows that 1.8 dB of the loss in the antenna at peak efficiency is due to the diodes, 1.6 dB is due to loss in the substrate, while the other 0.2 dB is due to matching differences between the feed and the cavity interior and reflections from the FSS. As such, the antenna efficiency could be improved by choosing diodes with lower ESR and a substrate with a

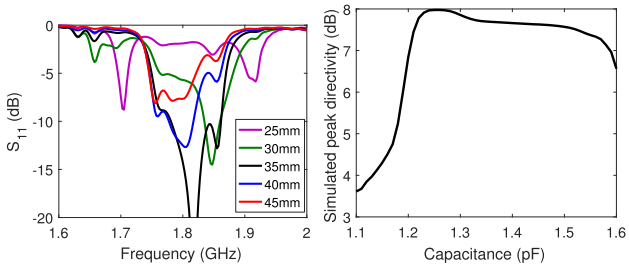

Fig. 9. (a) Simulated antenna S_{11} against frequency with different lengths of monopole probe l as a parameter. (b) Simulated directivity of antenna at 1.8 GHz with changing capacitance.

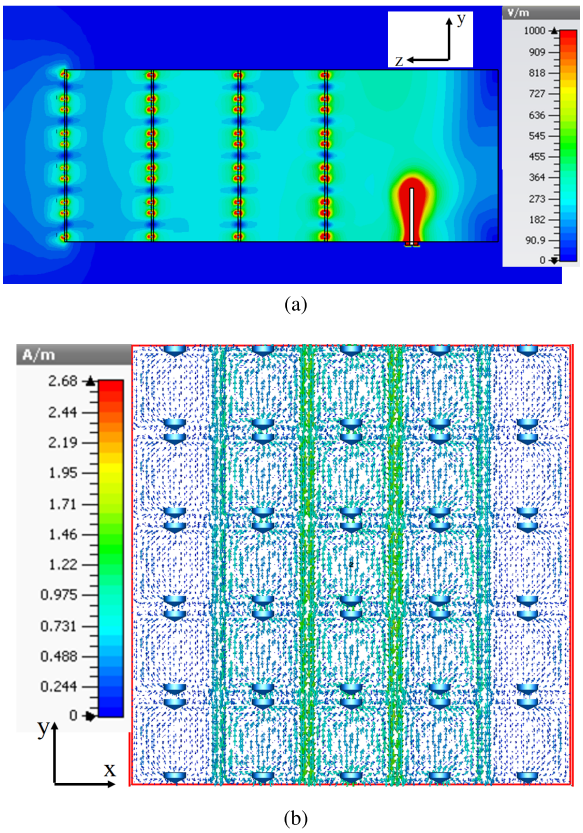

Fig. 10. (a) Simulated amplitude of electric field in antenna cross section. (b) Simulated surface currents on FSS 4 of antenna.

lower loss tangent. Some variation in the magnitude received at boresight is due to a slight change in the antenna pattern, as shown by the simulated boresight directivity in Fig. 9(b). It is mostly stable at 7.6 dB within the passband, but has a peak to 8 dB at 1.26 pF. This raises the received magnitude at boresight compared with the overall efficiency of the antenna at this capacitance. The simulated E-field distribution within the antenna at 1.35 pF is shown in Fig. 10(a), and the simulated surface currents on the final FSS layer are shown in Fig. 10(b).

IV. Experimental Results

A. Antenna Fabrication

The FSS was fabricated with standard PCB etching techniques, with copper conductor on 1.6 mm thick FR4 board.

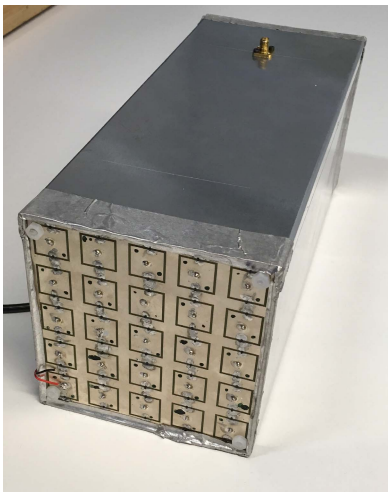

Fig. 11. Photograph of fabricated DAM unit.

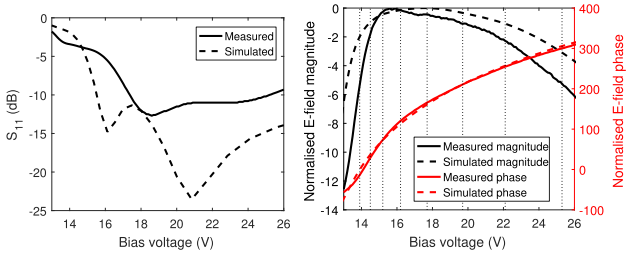

Fig. 12. Measured antenna with changing bias voltage. (a) Reflection coefficient at 1.8 GHz. (b) Normalized far-field magnitude and phase.

1SV280 varactor diodes were then soldered across the gaps of each FSS unit cell, all placed in line with the expected E-field. In order to fix the spacing of the FSS layers, holes were drilled in the corners of each FSS layer and a teflon threaded rod passed through, with teflon nuts holding each layer 57 mm from the next. The antenna cavity was fabricated from sheet aluminum, with a hole drilled for a panel-mount SMA connector with its center extended to 35 mm. Holes of 2 mm diameter were also drilled in the antenna side near where each FSS was to be placed to allow the biasing lines to be connected to wires, through RF chokes to a single coaxial cable for carrying the biasing signal. The cavity walls are held in place with conducting aluminum tape, and the final antenna is shown photographed in Fig. 11.

B. Antenna Measurement

The salient characteristics of the antenna were then measured, using a controllable voltage source to provide biasing. The antenna S_{11} was measured using a Agilent E5071C network analyzer in an anechoic chamber, and gives below 10 dB match for the majority of the antenna passband, though this is at some points reduced to 4 dB [Fig. 12(a)]. At these points the measured S_{11} departs from the simulated value markedly. This is because the antenna S_{11} is highly dependent on tolerances in the structure, in particular the length l of the monopole feed and the effective resistance of the diodes. The

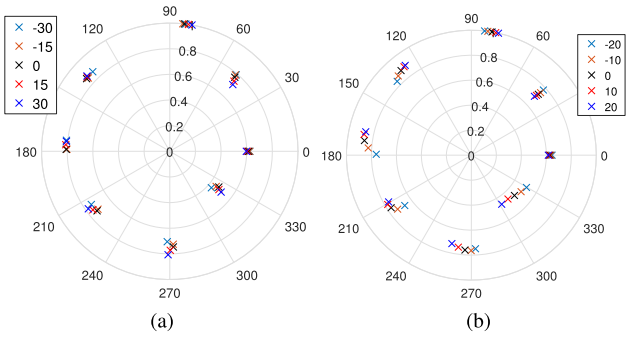

Fig. 13. 8PSK constellation produced by antenna at various viewing angles within beamwidth. (a) H-plane. (b) E-plane.

TABLE I
BIAS VOLTAGES FOR BPSK CONSTELLATION USING DAM

Data	Constellation point	Bias voltage (V)
0	-1	14.7
1	1	20.3

far-field magnitude and phase variation were measured with the network analyzer with a wideband horn antenna receiving the transmitted signals [Fig. 12(b)]. They show within the passband a drop in magnitude as bias voltage increases. Note that voltage is nonlinearly proportional to diode capacitance, accounting for the nonlinear change in phase across the passband, following closely the simulated phase change. The magnitude drops off steeper than expected on both sides of the peak, due to higher losses than expected, and also due to the higher S_{11} than expected.

There is 10.6 dB variation for 360° phase change, between 13.3 and 26.6 V, but most of this occurs in the final 29°. As such, an 8-PSK constellation, which requires 315° phase change, can be created with 5.3 dB variation between constellation points, shown by the dotted vertical lines in Fig. 12(b). The variation in transmitted magnitude between these bias points manifests as a constellation with reduced amplitude at some angles, as shown in Fig. 13. The constellation point on the positive real axis is produced by the minimum bias voltage 13.9 V, and increasing the bias voltage increases the transmitted phase from here (anticlockwise rotation). Fig. 13 also shows the variation in transmitted constellation observed over a range of viewing angles in both the E- and H-planes, showing a maximum of 15.6% variation in magnitude and 5.6° in phase for the H-plane over a 60° viewing angle. The E-plane beamwidth is smaller at 40°, and within this, has a maximum of 12.1% variation in magnitude and 22° in phase. The bias voltages required for BPSK, QPSK, and 8PSK are shown in Tables I–III, respectively.

The simulated and measured antenna radiation patterns are shown in Fig. 14 for the most and least transmissive constellation points measured. The peak gains differ between simulated and measured by 1.7 dB at maximum transmission (black curves) and 4.1 dB at minimum (red curves), showing a much steeper drop-off in magnitude at the edges of the response than expected. The measured beamwidth also decreases at extreme bias, from with a peak gain of 2.3 and 3 dB beamwidths of

TABLE II
BIAS VOLTAGES FOR QPSK CONSTELLATION USING DAM

Data	Constellation point	Bias voltage (V)
00	$1e^{-j3\pi/4}$	14.2
01	$1e^{j3\pi/4}$	23.5
10	$1e^{j\pi/4}$	15.7
11	$1e^{-j\pi/4}$	18.6

TABLE III
BIAS VOLTAGES FOR 8-PSK CONSTELLATION USING DAM

Data	Constellation point	Bias voltage (V)
000	1	22.1
001	$1e^{j\pi/4}$	25.3
010	$1e^{j3\pi/4}$	14.5
011	$1e^{j\pi/2}$	13.9
100	$1e^{-j\pi/4}$	19.7
101	$1e^{-j\pi/2}$	17.7
110	$1e^{j\pi}$	15.2
111	$1e^{-j3\pi/4}$	16.2

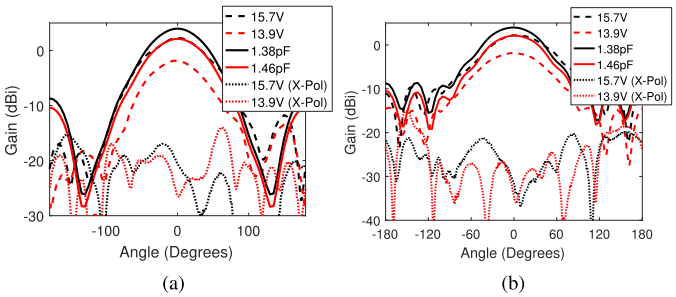

Fig. 14. Measured (voltage, dashed lines) and simulated (capacitance, solid lines) copolar and crosspolar (dotted lines) pattern of antenna at 1.8 GHz at peak and minimum transmission. (a) H-plane copolar. (b) E-plane copolar.

between 80° and 92° in the H-plane and 67° and 86° in the E-plane. This is due to the known deficiency in diode modeling for FSS applications, as manufacturer models are based on diodes being applied in microstrip transmission lines, rather than being embedded in an FSS orthogonal to the direction of power flow. Similar effects can be seen in [44]. All the crosspolar components produced within these beamwidths are at least 14.2 dB below the copolar magnitude at that angle.

V. SYSTEM IMPLEMENTATION OF MODULATING ANTENNA

In order to demonstrate the functionality of the fabricated modulating antenna, it was integrated into an end-to-end communications system. BER, symbol error rate (SER), packet error rate (PER) and error vector magnitude (EVM) measurements were taken.

A. Description of End-to-End Communications System With Modulating Antenna

The system diagram of the communications system is shown in Fig. 15. Random binary data is generated on a PC in MATLAB, and then processed to produce a string of modulated symbols. These symbols are multiplied by a pulse-shaping sequence $c(t)$, which here, is either a rectangular

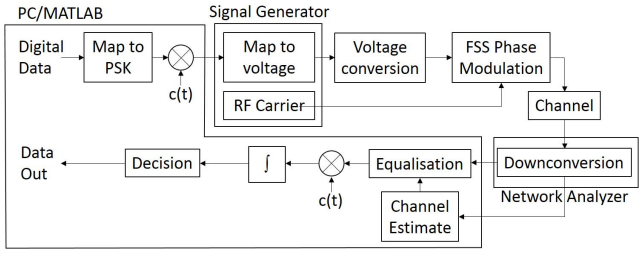

Fig. 15. System diagram for implementation of modulating antenna.

pulse represent by $c(t) = ((rect(t))/T_c)$, where $rect(t)$ is the rectangular function and T_c is the chip period; or a Manchester code pulse, where $c(t) = [1, -1] \cdot ((rect(t))/T_c)$. Using the Manchester code halves the throughput of the system, but means each PSK data symbol is composed of two PSK chips which will have different magnitudes when produced by DAM. This allows the magnitude variations to be averaged out at the receiver. Each data packet contained 1000 Bytes of data, which was preceded by a BPSK pilot sequence consisting of 50 iterations of the length 15 m-sequence.

The data chips are then sent to a Rohde & Schwarz SMBV100a signal generator, which maps the modulated data onto a nonlinear voltage between -1 and 1 V. This is then converted by some simple electronics into a bias voltage signal and connected by coaxial cable to the FSSs in the antenna. The 1.8 GHz RF carrier wave is also provided by the signal generator, and is connected to the antenna's RF feed. The antenna is placed facing into an anechoic chamber to ensure a simple AWGN channel, with a receiving horn antenna at boresight 1 m away. The horn antenna is connected to a Rohde & Schwarz FSV Spectrum Analyzer, which samples the signal and sends this data to MATLAB in the PC. The received pilot sequence is correlated with the m-sequence to estimate a complex number defining the channel [6]. The conjugate of this channel estimate is multiplied with the received data chips to equalize the channel effects, and these equalized chips are then multiplied by the pulse shaping sequence $c(t)$ and integrated over the symbol period T_s to recover the data symbols. A minimum distance detector was used to demodulate the symbols into binary data.

B. Measurement of System in AWGN

The setup measurement was performed in an anechoic chamber to minimize reflections and interference. The constellations produced are shown in Fig. 16, with $c(t)$ as a rectangular pulse and as a Manchester code. The constellations shown are for BPSK, QPSK and 8-PSK, with transmission at 1 Msymbol/s and a constant E_b/N_0 of 52 dB. The amplitude variation between constellation points is 1.1 dB for BPSK, 4.4 dB for QPSK, and 8.5 dB for 8-PSK. When a Manchester code is used, these reduce to 0.03 dB for BPSK, 1.8 dB for QPSK and 2.0 dB for 8-PSK, due to the averaging of the magnitude variation. It should also be noted that the EVM of the DAM constellation is noticeably larger than expected, with values of 7.4%, 8.3%, and 8.2% for BPSK, QPSK and 8-PSK, respectively. However, this reduces significantly when the Manchester code is used, to 2.3%, 4.0%, and 2.4%.

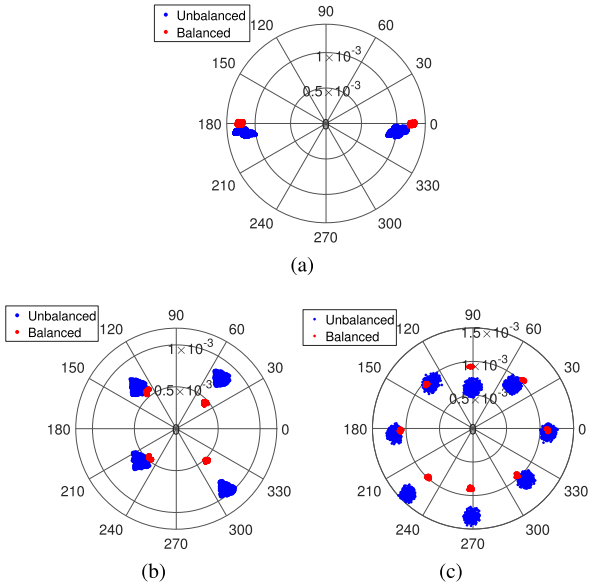

Fig. 16. Measured constellations produced by DAM in AWGN, Eb/N0 = 52 dB, balanced and unbalanced. (a) BPSK. (b) QPSK. (c) 8-PSK.

This suggests the variation is deterministic, and most likely caused by imperfections in the biasing signal sent to the direct antenna modulator. As such, improved driving of the antenna may improve the EVM further.

BER measurements are taken for each modulation scheme, with and without using a Manchester code, and compared against instrument grade modulation from the SMBV1000a signal generator over the same channel (Fig. 17). For demonstration, the transmitter sample rate in each case is 1 Msymbols/s. At each transmit power level, measurements were taken until 200 bit errors were observed and at least 10 packet errors were detected. The E_b/N_0 was calculated by comparing the noise power to the average signal power across 100 different packets at the signal generator's maximum transmit power to find a baseline. For BPSK, without balancing the DAM transmitter requires 2 dB more transmit power to achieve a BER of 10^{-5} compared with instrument grade modulation, whereas using a balancing sequence reduces this to nearly 0 dB. For QPSK, the difference is approximately 1.5 dB without balance, and 0.5 dB with balance. Unbalanced 8-PSK has an error rate which is only reducible to 10^{-4} due to the distortion of the constellation, which in many practical communications systems would be considered poor. However, using a balancing sequence allows performance only 1.5 dB worser at a BER of 10^{-5} and reduction below 10^{-6}. As such, the 8-PSK transmission can be used in practical line-of-sight scenarios. Across all modulation orders, the instrument grade modulation follows the theoretical BER curve, showing the quality of this modulation, compared with the prototype DAM transmitter, which has some degradation, which increases with the modulation order.

This demonstrates significant advances over previous demonstrations of DAM using FSS [29]. By using four FSS layers rather than three, this work has increased the modulation order achievable from QPSK to 8-PSK. Compared with other DAM approaches, as shown in Table IV, this is equivalent

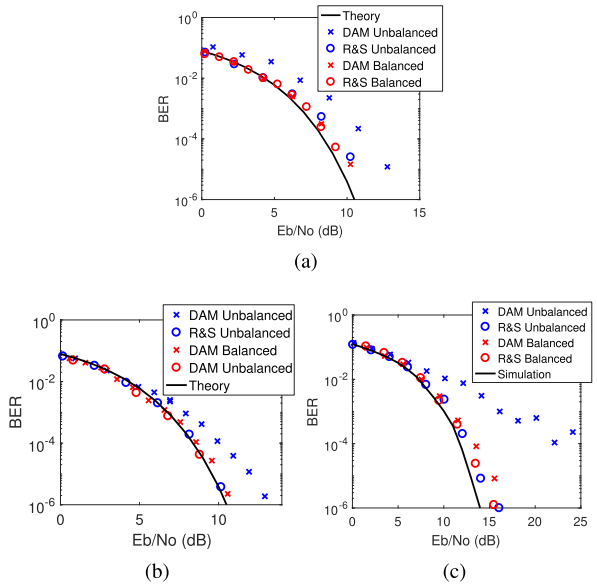

Fig. 17. Measured BERs for DAM and instrument grade modulation in AWGN, balanced, and unbalanced. (a) BPSK. (b) QPSK. (c) 8-PSK.

TABLE IV
COMPARISON OF KEY METRICS FOR DAM TECHNIQUES

DAM technique	Modulation format	Operating Frequency (GHz)	Symbol rate (MSymbol/s)	Physical dimensions (λ^3)
This paper	8PSK	1.8	1	0.68×0.68×1.71
[29]	QPSK	1.8	1	0.53×0.53×1.02
[27]	8PSK	4.25	2.048	5.44×1.36×0.07
[20]	OOK	1	5	0.32×0.39×0.01

to the modulation orders achieved by [27] and an advance over [20]. However, this comes at the cost of a greater physical depth than all the other approaches, reaching 1.71λ. This is still much smaller than the largest dimension of [27], which uses a metasurface of $5.44 \times 1.36 \times 0.07\lambda^3$. It should also be noted that [27] requires a plane wave feed to the metasurface, which is not included in the dimensions given here. The solution in [20] is the most compact, at nearly a quarter of the aperture area of the DAM unit in this article.

Compared with [29], the use of diodes with lower series resistance has improved the peak antenna efficiency from 10% to 46%. However, efficiency results are not given in [20] and [27]. The symbol rate demonstrated in this article is of a similar order to, but lower than, that achieved in [20] and [27], though the same as [29]. Note, however, that these values are those demonstrated by practical testbeds, which are not necessarily the upper limits of each technique's operation. Also, the carrier frequencies of each approach, which range from 1 to 4.25 GHz, are those chosen for the design of these testbeds, and each approach is unlikely to be limited to only those given frequencies. Finally, while [29] uses a spreading code of length 15 to ameliorate the magnitude variation caused by FSS modulation, this article demonstrates good performance for BPSK and QPSK with no ameliorating technique, and amelioration of 8-PSK with a Manchester code, which has length 2. This increases the data throughput in the same bandwidth. The sum effect of these advances is a smaller difference in BER performance between DAM and conventional modulation. Furthermore, this article is, to the authors' knowledge, the only demonstration of DAM reaching BER performance of 10^{-6}.

In all, this work has demonstrated a DAM solution with comparable symbol rates and operating frequencies to existing solutions. It has a smaller form factor than [27], while producing higher order modulation than [29] and [20].

VI. CONCLUSION

The first FSS-based direct antenna modulator capable of producing phase modulation up to 8-PSK has been presented, designed, characterized, and tested in an end-to-end communication system. The designed antenna was simulated to have a peak efficiency of 46% and magnitude variation of 2.7 dB over 360° of phase change. Measurement found a peak gain of 2.3 dB, and 6 dB variation for 315° of phase change. The transmitted constellation was consistent in magnitude and phase within the antenna 3 dB beamwidth of 60° in the H-plane and 40° in the E-plane. When a balancing code is used, the DAM transmitter produces constellations with EVM of the order of 2%. The BER performance of the DAM transmitter, when compared with instrument grade modulation, is impaired by 0, 2, and 1.5 dB for binary, quaternary and 8-PSK, respectively. Future work will examine the effects of lower loss materials, explore the possibility of amplitude modulation, and implement DAM in multipath communications systems.

ACKNOWLEDGMENT

Data deposit link https://doi.org/10.15131/shef.data.9735278.

REFERENCES

[1] M. R. Palattella *et al.*, "Internet of Things in the 5G era: Enablers, architecture, and business models," *IEEE J. Sel. Areas Commun.*, vol. 34, no. 3, pp. 510–527, Mar. 2016.
[2] Y.-P. E. Wang *et al.*, "A primer on 3GPP narrowband Internet of Things," *IEEE Commun. Mag.*, vol. 55, no. 3, pp. 117–123, Mar. 2017.
[3] A. Woolhouse. (2018). *The Weightless Standard*. [Online]. Available: http://wireless.ictp.it/tvws/book/11.pdf
[4] T. J. Myers, "Random phase multiple access system with meshing," U.S. Patent 7 773 664 B2, Aug. 10, 2010.
[5] A. Augustin, J. Yi, T. Clausen, and W. M. Townsley, "A study of LoRa: Long range & low power networks for the Internet of Things," *Sensors*, vol. 16, no. 9, p. 1466, 2016. [Online]. Available: http://www.ncbi.nlm.nih.gov/pmc/articles/PMC5038744/
[6] A. Goldsmith, *Spread Spectrum for Wireless Communications*. Cambridge, U.K.: Cambridge Univ. Press, 2005.
[7] R. Boisguene, S.-C. Tseng, C.-W. Huang, and P. Lin, "A survey on NB-IOT downlink scheduling: Issues and potential solutions," in *Proc. 13th Int. Wireless Commun. Mobile Comput. Conf. (IWCMC)*, Jun. 2017, pp. 547–551.
[8] A. Arbi and T. O'Farrell, "Energy efficiency in 5G access networks: Small cell densification and high order sectorisation," in *Proc. IEEE Int. Conf. Commun. Workshop (ICCW)*, Jun. 2015, pp. 2806–2811.
[9] W. Guo and T. O'Farrell, "Capacity-energy-cost tradeoff in small cell networks," in *Proc. IEEE 75th Veh. Technol. Conf. (VTC Spring)*, May 2012, pp. 1–5.
[10] A. Behzad, *Radio Receiver and Transmitter Architectures*. Hoboken, NJ, USA: Wiley, 2008, p. 224. [Online]. Available: http://ieeexplore.ieee.org/xpl/articleDetails.jsp?arnumber=5224911
[11] S. C. Cripps, *RF Power Amplifiers for Wireless Communications* (Artech House Microwave Library Hardcover), 2nd ed. Norwood, MA, USA: Artech House, 2006.
[12] *GSM/EDGE Modulation*, document 3GPP, 3rd Generation Partnership Project (3GPP), Technical Specification (TS) 45.004, 06 2001, version 4.0.0, Feb. 2016. [Online]. Available: https://portal.3gpp.org/desktopmodules/Specifications/SpecificationDetails.aspx?specificationId=2708

[13] K. Murota and K. Hirade, "GMSK modulation for digital mobile radio telephony," *IEEE Trans. Commun.*, vol. COM-29, no. 7, pp. 1044–1050, Jul. 1981.
[14] W. H. Doherty, "A new high efficiency power amplifier for modulated waves," *Proc. IRE*, vol. 24, no. 9, pp. 1163–1182, Sep. 1936.
[15] T. W. Barton and D. J. Perreault, "Theory and implementation of RF-input outphasing power amplification," *IEEE Trans. Microw. Theory Techn.*, vol. 63, no. 12, pp. 4273–4283, Dec. 2015.
[16] H. Jang *et al.*, "RF-input self-outphasing Doherty–Chireix combined amplifier," *IEEE Trans. Microw. Theory Techn.*, vol. 64, no. 12, pp. 4518–4534, Dec. 2016.
[17] V. F. Fusco and Q. Chen, "Direct-signal modulation using a silicon microstrip patch antenna," *IEEE Trans. Antennas Propag.*, vol. 47, no. 6, pp. 1025–1028, Jun. 1999.
[18] S. D. Keller, W. D. Palmer, and W. T. Joines, "Electromagnetic modeling and simulation of a directly modulated patch antenna," *IEEE Antennas Wireless Propag. Lett.*, vol. 9, pp. 779–782, 2010.
[19] S. D. Keller, W. D. Palmer, and W. T. Joines, "Switched antenna circuit with increased information bandwidth," *IEEE Antennas Wireless Propag. Lett.*, vol. 9, pp. 1045–1048, 2010.
[20] S. Srivastava and J. J. Adams, "Analysis of a direct antenna modulation transmitter for wideband OOK with a narrowband antenna," *IEEE Trans. Antennas Propag.*, vol. 65, no. 10, pp. 4971–4979, Oct. 2017.
[21] A. Babakhani, D. B. Rutledge, and A. Hajimiri, "Transmitter architectures based on near-field direct antenna modulation," *IEEE J. Solid-State Circuits*, vol. 43, no. 12, pp. 2674–2692, Dec. 2008.
[22] A. Babakhani, D. B. Rutledge, and A. Hajimiri, "Near-field direct antenna modulation," *IEEE Microw. Mag.*, vol. 10, no. 1, pp. 36–46, Feb. 2009.
[23] H. Shi and A. Tennant, "Simultaneous, multichannel, spatially directive data transmission using direct antenna modulation," *IEEE Trans. Antennas Propag.*, vol. 62, no. 1, pp. 403–410, Jan. 2014.
[24] M. P. Daly and J. T. Bernhard, "Directional modulation technique for phased arrays," *IEEE Trans. Antennas Propag.*, vol. 57, no. 9, pp. 2633–2640, Sep. 2009.
[25] G. I. Kiani, T. S. Bird, and K. Lee Ford, "60 GHz ASK modulator using switchable FSS," in *Proc. IEEE Antennas Propag. Soc. Int. Symp. (APSURSI)*, Jul. 2010, pp. 1–4.
[26] T. K. Chang, R. J. Langley, and E. Parker, "An active square loop frequency selective surface," *IEEE Microw. Guided Wave Lett.*, vol. 3, no. 10, pp. 387–388, Oct. 1993.
[27] W. Tang *et al.*, "Programmable metasurface-based RF chain-free 8PSK wireless transmitter," *Electron. Lett.*, vol. 55, no. 3, pp. 417–420, Apr. 2019.
[28] S. Henthorn, K. Lee Ford, and T. O'Farrell, "Frequency selective surface loaded antenna for direct antenna modulation," in *Proc. 11th Eur. Conf. Antennas Propag. (EUCAP)*, Mar. 2017, pp. 731–734.
[29] S. Henthorn, K. Lee Ford, and T. O'Farrell, "Bit-error-rate performance of quadrature modulation transmission using reconfigurable frequency selective surfaces," *IEEE Antennas Wireless Propag. Lett.*, vol. 16, pp. 2038–2041, 2017.
[30] A. H. Abdelrahman, F. Yang, A. Z. Elsherbeni, P. Nayeri, and C. A. Balanis, *Analysis and Design of Transmitarray Antennas*. San Rafael, CA, USA: Morgan & Claypool, 2017. [Online]. Available: http://ieeexplore.ieee.org/xpl/articleDetails.jsp?arnumber=7833475
[31] A. Epstein, J. P. S. Wong, and G. V. Eleftheriades, "Cavity-excited Huygens' metasurface antennas for near-unity aperture illumination efficiency from arbitrarily large apertures," *Nature Commun.*, vol. 7, Jan. 2016, Art. no. 10360. doi: 10.1038/ncomms10360.
[32] J. R. Reis *et al.*, "FSS-inspired transmitarray for two-dimensional antenna beamsteering," *IEEE Trans. Antennas Propag.*, vol. 64, no. 6, pp. 2197–2206, Jun. 2016.
[33] M. Sazegar *et al.*, "Beam steering transmitarray using tunable frequency selective surface with integrated ferroelectric varactors," *IEEE Trans. Antennas Propag.*, vol. 60, no. 12, pp. 5690–5699, Dec. 2012.
[34] A. Clemente, L. Dussopt, R. Sauleau, P. Potier, and P. Pouliguen, "1-bit reconfigurable unit cell based on PIN diodes for transmit-array applications in x-band," *IEEE Trans. Antennas Propag.*, vol. 60, no. 5, pp. 2260–2269, May 2012.
[35] F. Diaby *et al.*, "Linearly-polarized electronically reconfigurable transmitarray antenna with 2-bit phase resolution in Ka-band," in *Proc. Int. Conf. Electromagn. Adv. Appl. (ICEAA)*, Sep. 2017, pp. 1295–1298.
[36] R. J. Langley and E. A. Parker, "Equivalent circuit model for arrays of square loops," *Electron. Lett.*, vol. 18, no. 7, pp. 294–296, Apr. 1982.
[37] O. Bayraktar, O. A. Civi, and T. Akin, "Beam switching reflectarray monolithically integrated with RF MEMS switches," *IEEE Trans. Antennas Propag.*, vol. 60, no. 2, pp. 854–862, Feb. 2012.
[38] M. Haghzadeh, L. M. Bhowmik, C. Armiento, and A. Akyurtlu, "Printed tunable miniaturized frequency selective surface with BST/polymer composite filled interdigital capacitors," in *Proc. USNC-URSI Radio Sci. Meeting (Joint AP-S Symp.)*, Jul. 2014, p. 154.
[39] W. Hu *et al.*, "Liquid crystal tunable mm wave frequency selective surface," *IEEE Microw. Wireless Compon. Lett.*, vol. 17, no. 9, pp. 667–669, Sep. 2007.
[40] A. H. Abdelrahman, A. Z. Elsherbeni, and F. Yang, "Transmission phase limit of multilayer frequency-selective surfaces for transmitarray designs," *IEEE Trans. Antennas Propag.*, vol. 62, no. 2, pp. 690–697, Feb. 2014.
[41] Toshiba. (2014). *1SV280 Variable Capacitance Diode*. [Online]. Available: https://toshiba.semicon-storage.com/info/docget.jsp?did=2796&prodName=1SV280
[42] N. Marcuvitz, *Waveguide Handbook*. London, U.K.: Institution of Electrical Engineers, 1986.
[43] NOKIA. (2017). *LTE Evolution for IOT Connectivity*. [Online]. Available: https://resources.ext.nokia.com/asset/200178
[44] J. Roberts, K. Lee Ford, and J. M. Rigelsford, "Secure electromagnetic buildings using slow phase-switching frequency-selective surfaces," *IEEE Trans. Antennas Propag.*, vol. 64, no. 1, pp. 251–261, Jan. 2016.

Stephen Henthorn received the M.Eng. degree (Hons.) in electronic and communications engineering from The University of Sheffield, Sheffield, U.K., in 2015, where he is currently pursuing the Ph.D. degree with the Department of Electronic and Electrical Engineering.

He received the Professor Sharom Ahmat Prize for the performance in the final year of his master's degree. His current research interests include reconfigurable antennas and metamaterials, and their applications in wireless communications systems.

Kenneth Lee Ford (M'07–SM'10) received the B.Eng. and Ph.D. degrees in electronic engineering from The University of Sheffield, Sheffield, U.K. in 1998 and 2003, respectively.

In 2001, he joined the Stealth Materials Department, Advanced Technology Centre, BAE Systems, Towcester, U.K. In 2005, he joined The University of Sheffield, as a Lecturer of communications, where he became a Senior Lecturer in 2012. His current research interests include reconfigurable antennas, miniaturized antennas, metamaterials, propagation in the built environment, and electromagnetic structures for biomedical applications.

Timothy O'Farrell (M'91–SM'18) received the M.Sc. (Hons.) and Ph.D. degrees from The University of Manchester, Manchester, U.K., in 1986 and 1989, respectively.

From 2009 to 2012, he was with the Mobile VCE (mVCE), where he was the Academic Coordinator of the Core 5 Green Radio Project and a Leader in establishing energy efficiency as a global research field in wireless communication systems. He is currently leading the FARAD Project and the U.K. Research Strategy Community Organisation in Communications, Mobile Computing, and Networking within the EPSRC portfolio. He is currently the Chair Professor of wireless communications with The University of Sheffield, Sheffield, U.K. He has managed 26 major research projects as a Principal Investigator. He has authored 315 journals and conference papers, book chapters, patents, and technical reports, and has participated in standards, consultancy, and expert witness activities within the wireless sector. He has pioneered research on energy-efficient mobile cellular communications, the mathematical modeling of carrier sense multiple access-based MAC protocols for WiFi, coded modulation techniques for optical wireless communication systems, and spreading sequence design for CDMA wireless networks. His current research interests include wireless communication systems, especially physical layer signal processing, radio resource management, and wireless network planning.

Dr. O'Farrell is the Director of the Mobile VCE (mVCE), a Chartered Engineer, and a member of the IET.